Letter

Photoemission angular distribution beyond the single wavevector description of photoelectron final states

Hiroaki Tanaka,[1,*] Shota Okazaki,[2] Yuto Fukushima,[1] Kaishu Kawaguchi,[1] Ayumi Harasawa,[1] Takushi Iimori,[1] Fumio Komori,[3] Masashi Arita,[4] Ryo Mori,[1] Kenta Kuroda,[5,6,7,†] Takao Sasagawa,[2,8,‡] and Takeshi Kondo[1,9,§]

[1]*Institute for Solid State Physics, The University of Tokyo, Kashiwa, Chiba 277-8581, Japan*

[2]*Laboratory for Materials and Structures, Tokyo Institute of Technology, Yokohama, Kanagawa 226-8503, Japan*

[3]*Institute of Industrial Science, The University of Tokyo, Meguro-ku, Tokyo 153-8505, Japan*

[4]*Hiroshima Synchrotron Radiation Center, Hiroshima University, Higashi-hiroshima, Hiroshima 739-0046, Japan*

[5]*Graduate School of Advanced Science and Engineering, Hiroshima University, Higashi-hiroshima, Hiroshima 739-8526, Japan*

[6]*International Institute for Sustainability with Knotted Chiral Meta Matter (WPI-SKCM^2), Hiroshima University, Higashi-hiroshima, Hiroshima 739-8526, Japan*

[7]*Research Institute for Semiconductor Engineering, Hiroshima University, Higashi-hiroshima, Hiroshima 739-8527, Japan*

[8]*Research Center for Autonomous Systems Materialogy, Tokyo Institute of Technology, Yokohama, Kanagawa 226-8503, Japan*

[9]*Trans-scale Quantum Science Institute, The University of Tokyo, Bunkyo-ku, Tokyo 113-0033, Japan*

(Received 10 November 2023; revised 23 May 2024; accepted 28 May 2024; published 20 June 2024)

We develop a simulation procedure for angle-resolved photoemission spectroscopy (ARPES), where a photoelectron wave function is set to be an outgoing plane wave in a vacuum associated with the emitted photoelectron wave packet. ARPES measurements on the transition metal dichalcogenide $1T$-TiS_2 are performed, and our simulations exhibit good agreement with experiments. Analysis of our calculated final state wave functions quantitatively visualizes that they include various waves due to the boundary condition and the uneven crystal potential. These results show that a more detailed investigation of the photoelectron final states is necessary to fully explain the photon-energy- and light-polarization-dependent ARPES spectra.

DOI: 10.1103/PhysRevB.109.L241114

Angle-resolved photoemission spectroscopy (ARPES) has been a powerful method for investigating the electronic structure of solid crystals [1]. It is based on the photoelectric effect [2]; the energies and momenta of photoelectrons derive the band dispersion of a solid. As well as the band dispersion, the intensity distribution of ARPES spectra gives information on the wave function of each band because the matrix element between the ground state and the photoexcited state determines it. Particularly, the light polarization dependence of ARPES spectra has extracted the electronic structure information of various kinds of materials [3–8].

In response to growing interest in the photoemission angular distribution, numerical studies have reported its simulation methodologies [3,9–15]. We focus on calculating a photoemission matrix element derived from Fermi's golden rule; on the other hand, there has been another approach to ARPES spectra simulation by time-dependent density functional theory [16,17]. A plane wave is the simplest form for describing final states, and some studies have added the scattering effects for better reproducibility [17–19]. These studies have assumed that the photoelectron wave function in a solid is associated with a single wavevector $\mathbf{k} = (\mathbf{k}_\parallel, k_z)$ [Fig. 1(a)]; $\mathbf{k}_\parallel$ represents the in-plane (xy) components. This assumption is consistent with the three-step model of photoemission [20], where a photoelectron is described as a classical particle with a certain momentum. On the other hand, the time evolution analysis of photoemission has revealed that a photoelectron propagates as a wave packet, a cropped plane wave, in a vacuum [21]. The wavelike behavior of photoelectrons tells us that time-reversed low-energy electron diffraction (TR-LEED) states, which have been employed for decades [22,23], are appropriate for analyzing the whole amplitude of photoelectron wave packet (see Note 1 in Supplemental Material (SM) [24]); The LEED states are determined by the boundary condition that there is only the transmitted wave in the $z \to -\infty$ limit and the TR-LEED states are obtained by taking the time reversal of them. Since TR-LEED states are determined by the boundary condition at the vacuum layer below the slab, one needs to calculate the TR-LEED wave function for the entire range of the thick slab, leading to a large numerical error in the near-surface region, which is crucial for analyzing surface-sensitive photoemission. One method to avoid this difficulty is to add an imaginary constant optical potential, making the photoelectron wave function rapidly decay into bulk [25–29]. However, a recent ARPES study on layered materials has reported that the exponential decay associated with the constant optical potential cannot reproduce the ARPES spectra modulation by the surface sensitivity [30].

In this Letter, we propose another approach to the photoemission simulation within the Kohn-Sham system of the density functional theory [45,46] by approximating the photoelectron wave function to include only an outgoing plane wave in the vacuum above the slab [pink curve in Fig. 1(b)].

*Contact author: hhiiro2022@gmail.com
†Contact author: kuroken224@hiroshima-u.ac.jp
‡Contact author: sasagawa@msl.titech.ac.jp
§Contact author: kondo1215@issp.u-tokyo.ac.jp

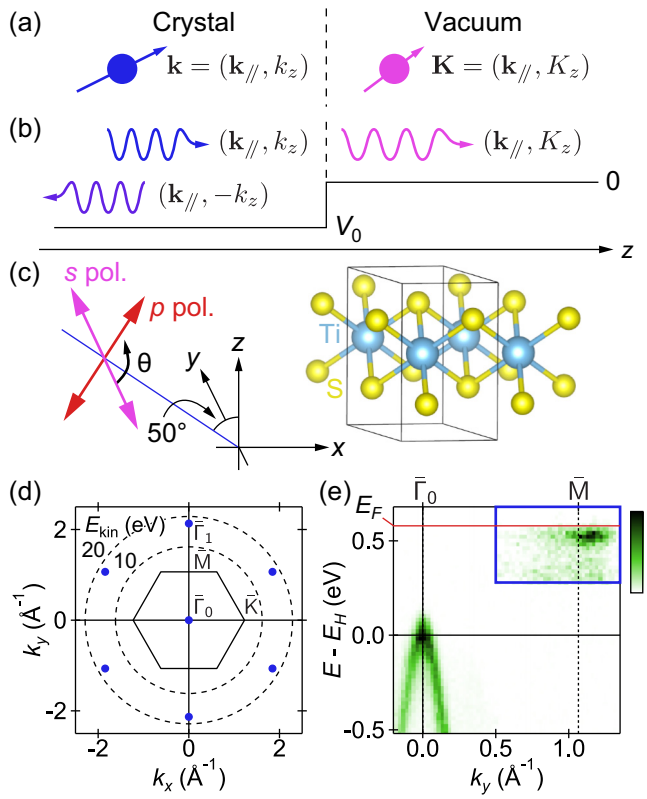

FIG. 1. Description of the photoemission process and fundamental properties of $1T$-TiS_2. (a) Three-step model description of the photoemission. (b) Schematic of a photoelectron wave function discussed in the present Letter. (c) Crystal structure and incident light direction in ARPES measurements. (d) Brillouin zone (black hexagon) and reciprocal lattice points (blue dots). Black dashed circles represent the wavevector length satisfying $E_{\rm kin} = \hbar^2 k^2/2m$. (e) Experimental band dispersion along the k_y direction taken by 35 eV synchrotron light.

This approximation removing the ingoing plane waves is supported by our one-dimensional photoemission simulations (Fig. S3 in SM [24]). In this situation, the photoelectron wave function inside a solid can contain various waves other than the traveling wave. Even in the stepped potential model, the connection condition at the boundary requires the wave function to include the reflected wave $(\mathbf{k}_\parallel, -k_z)$ [purple curve in Fig. 1(b)]. Consequently, the photoemission angular distribution using such final-state wave functions can differ from that using the three-step model wave function, including only the traveling wave; we refer to them as first-principles (FP) and plane-wave (PW) final states, respectively. Our photoemission intensity calculations were validated by comparing them with ARPES spectra of the transition-metal dichalcogenide (TMD) $1T$-TiS_2 [Fig. 1(c)]. While the electronic structure of TMDs has been investigated by ARPES [47–50], $1T$-TiS_2 is ideal for our study because of the easily cleavable quasi-two-dimensional structure, no need for considering the termination surface dependence [51], and the simple electronic structure without the charge density wave phase in contrast to other $1T$-type TMDs [52]. We found that the intensity distributions of FP final states were closer to experimental ones than those of PW final states. Moreover, our wave component analysis of FP wave functions demonstrated that they include various plane waves beyond just the traveling wave; these components, absent in the PW final states, contributed to a better agreement between experiments and simulations. Our study is a quantitative demonstration that the final-state wave functions include reflected waves in a solid. Our study provides a precise description of the photoemission process, which can be particularly important when extracting physical quantities from photoemission angular distribution.

Single crystals of $1T$-TiS_2 were grown by the chemical vapor transport method with iodine as the transport agent. Magnetotransport and x-ray photoemission measurements exhibited only trivial behavior, indicating the simple electronic structure of this material (Notes 2 and 3 in SM [24]). Laue back-reflection measurements determined the crystal geometry as described in Fig. 1(c) (Note 4 in SM [24]). ARPES measurements using a 7-eV laser and synchrotron radiation ($h\nu = 9$–39 eV) were performed at ISSP, the University of Tokyo [53,54] and HiSOR BL-9A, respectively (Note 5 in SM [24]). $1T$-TiS_2 possesses a hole band around the $\bar{\Gamma}$ point and an electron band around the $\bar{M}$ point, forming an indirect band gap [Fig. 1(e)]. We focus on the hole band in discussing the photoemission intensity; we represent its top position by E_H and use it as the base point of the energy axis.

Before presenting the experimental results, we explain the calculation procedure for the FP final states. We implemented the FP wave function calculations in SPADExp [15], which uses OpenMX [34] to calculate the ground state wave functions and the Kohn-Sham potential. The ground state electronic structure for a 40-layer slab without surface relaxation (Note 7 in SM [24]) was obtained using the Perdew-Burke-Ernzerhof (PBE) functional [38,39]. Although the system becomes semimetallic due to the band-gap underestimation of the PBE functional (Note 6 in SM [24]), the overall shape of the quasi-two-dimensional hole band around the $\bar{\Gamma}$ point agrees well with experimental results. See Note 8 in SM [24] for other calculation properties.

The FP wave functions are calculated using the local part of the Kohn-Sham potential and the kinetic energy value; the latter is determined by the binding energy of the ground state, the incident photon energy, and the work function. Owing to the in-plane periodicity of the system, the wave function can be Fourier expanded,

$$\psi^F(\mathbf{r}) = \sum_{\mathbf{g}_\parallel} e^{i(\mathbf{k}_\parallel + \mathbf{g}_\parallel)\cdot \mathbf{r}_\parallel} \cdot \psi_{\mathbf{g}_\parallel}(z), \tag{1}$$

where $\mathbf{r} = (\mathbf{r}_\parallel, z)$ holds and $\mathbf{g}_\parallel$ represents an in-plane reciprocal lattice vector, corresponding to the blue dots in Fig. 1(d). This representation is available both in a solid and a vacuum. The Fourier-expanded potential is also periodic along the z direction inside the crystal except for the top and bottom layers [Fig. 2(a)]. Therefore, the wave function in the region is the linear combination of the bulk wave function,

$$\psi^F(\mathbf{r}) = \sum_n p_n \psi_n^{\rm bulk}(\mathbf{r}), \quad \psi_n^{\rm bulk}(\mathbf{r}) = \sum_{\mathbf{g}} e^{i(\mathbf{k}_n + \mathbf{g})\cdot \mathbf{r}} \cdot \psi_{n\mathbf{g}}, \tag{2}$$

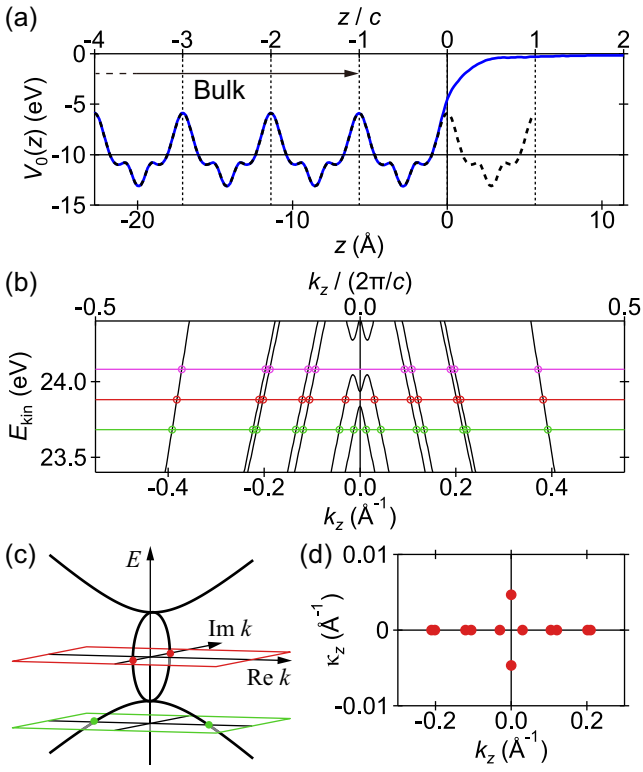

FIG. 2. FP wave function calculations. (a) $\mathbf{g}_\parallel = 0$ component of the Fourier-expanded potential. The $1T$-TiS_2 slab is placed in the $z < 0$ region. Black dashed curves and solid horizontal lines represent the periodic bulk potential and its $\mathbf{g} = 0$ component. (b) Bulk band dispersion of unoccupied states along the real k_z axis. The in-plane momentum is set to $(0.1, 0.0)$ (Å^{-1}). (c) Band dispersion of the effective model around the hybridization gap. Only the real eigenvalues are plotted. The constant-energy planes colored red and green correspond to the horizontal lines in (b). (d) Magnified view of the z component distribution with the kinetic energy corresponding to the red line in (b).

where n is the band index, $\mathbf{g} = (\mathbf{g}_\parallel, g_z)$ is a bulk reciprocal vector, and $\psi_{n\mathbf{g}}$ is a number representing an eigenstate. Equation (2) is available only in the bulk region.

The z component of the wavevector $\mathbf{k}_n$ is determined so that the eigenenergy equals the specified kinetic energy and is not limited to a real value because of the incomplete translational symmetry of the slab system along the z direction; $\mathbf{k}_n$ can be decomposed as $(\mathbf{k}_\parallel, k_{nz} - i\kappa_{nz})$. The complex z component is necessary when the specified kinetic energy is located within a hybridization gap of the unoccupied band dispersion [red and pink lines in Fig. 2(b)]. In these cases, the number of eigenstates on the real k_z axis is fewer than otherwise [green line in Fig. 2(b)], making them insufficient as a basis set. Considering the effective Hamiltonian around the hybridization gap $H(k) = \begin{pmatrix} ak & t \\ t & -ak \end{pmatrix}$ and extend k into the complex plane, we can find two bands within the hybridization gap [Fig. 2(c)]. While two eigenstates are on the real k_z axis when the specified kinetic energy is out of the gap [green dots in Fig. 2(c)], they are on the complex plane when the kinetic energy is within the gap [red dots in Fig. 2(c)]. Also in the case of the unoccupied states in Fig. 2(b), we find two eigenstates with complex z components for each gapped dispersion pair [Figs. 2(d) and S10 in SM [24]]. The other case happens when $\mathbf{g}_\parallel$ and κ_z are relatively large, but it only weakly affects the FP wave function (Note 9 in SM [24]). The linear combination coefficient p_n and the wave function of the top layer are determined to satisfy the Schrödinger equation and the boundary condition in a vacuum; $\psi_{\mathbf{g}_\parallel}(z)$ is equal to $e^{iK_z z}$ when $\mathbf{g}_\parallel = 0$ and to zero otherwise. After these calculations, the decay function is multiplied to effectively include the surface-sensitive property of photoemission spectroscopy (Ref. [55] and Note 8 in SM [24]). We note that the projector-type nonlocal component of pseudopotentials [56], which affects the wave function around the nuclei, is omitted in the FP wave-function calculations for the stability and computational cost reduction (Note 10 in SM [24]).

We applied the FP wave functions to simulate the photoemission angular distribution of $1T$-TiS_2 and compared the results with experimental spectra. Experimental ARPES spectra using synchrotron light strongly depended on the incident photon energy and polarization [Figs. 3(a), 3(b), S11, and S12 in SM [24]], indicating that the photoemission matrix element strongly depends on those conditions. The s-polarization spectra were symmetric, as both the crystal structure and the light electric field are symmetric with respect to the yz plane, while p-polarized spectra were not. We determined the degree of asymmetry $(I_+ - I_-)/(I_+ + I_-)$, where $I_\pm$ represents the integrated photoemission intensity at $k_x = \pm 0.1$ Å^{-1} [dashed lines in Figs. 3(a) and 3(b)]. For the s-polarized light, the degree of asymmetry was nearly zero across the whole photon energy range. On the other hand, the degree of asymmetry for the p-polarized light varied significantly with the photon energy [Fig. 3(c)], while its momentum dependence was weak (Fig. S13 in SM [24]). This strongly varying behavior indicates that the degree of asymmetry is one proper quantity to discuss the photoemission matrix element.

Photoemission intensity simulations using the FP wave functions could reproduce similar trends as shown in Fig. 3(h). In the calculations, the light polarization affects the photoemission intensity as the vector potential direction in the matrix element. We found that the aforementioned method for FP final states becomes unstable at the incident photon energies below 25 eV (Note 10 in SM [24]). In this case, we limited the $\mathbf{g}_\parallel$ vector within the circle determined by the kinetic energy [Fig. 1(d)] and solved the ordinal differential equation for the slab wave function [Eq. (1)]. The $\mathbf{g}_\parallel$-limited calculations [blue curve in Fig. 3(h)] were also applicable for photon energies greater than 25 eV while the $\mathbf{g}_\parallel$-unlimited version [purple curve in Fig. 3(h)] was suitable for the photon energy between 25 and 40 eV. Both calculations exhibited very similar dispersions within this range, suggesting the large $\mathbf{g}_\parallel$ component is not so considerable. Comparing the PW and FP final states, we claim that the FP final states exhibit better agreement with the sharp local minimum observed around $h\nu = 20$ eV and larger positive asymmetry in $h\nu = 35$–40 eV. The latter difference is clearly visualized in Figs. 3(f) and 3(g) for $h\nu = 37$ eV, corresponding to Fig. 3(b).

In laser ARPES measurements, we could investigate the polarization dependence in more detail by continuously changing the polarization angle θ in Fig. 1(c). The s- and p-polarization spectra showed similar behavior to

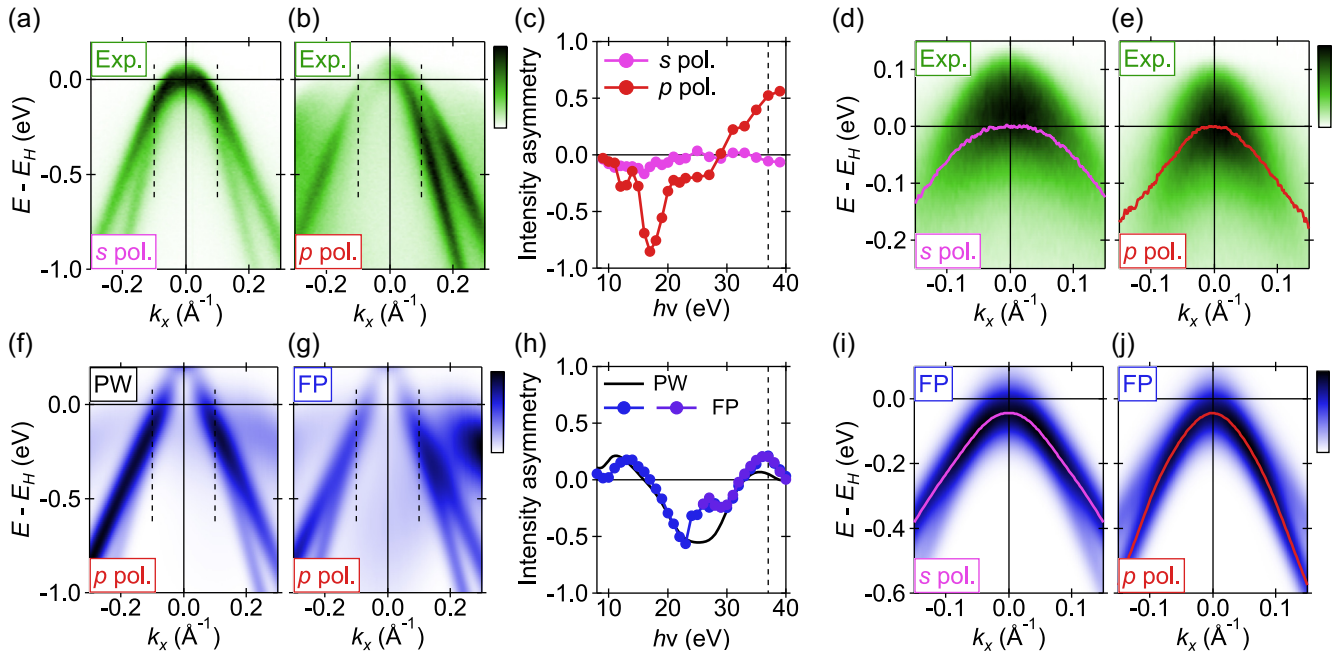

FIG. 3. Experimental ARPES spectra and simulation results. (a), (b) Experimental spectra along the k_x direction taken by s- and p-polarized 37 eV synchrotron lights, respectively. (c) Photon energy dependence of the integrated intensity asymmetry along the dashed lines in (a) and (b). The vertical dashed line is located at $h\nu = 37$ eV. (d), (e) ARPES spectra taken by the 7 eV laser. The overlaid curves represent peak positions extracted from energy distribution curves. (f), (g) Simulated photoemission angular distribution using the PW and FP final states. The incident light was 37 eV, p polarized. (h) Integrated intensity asymmetry calculated from simulated spectra. The blue and purple curves represent the FP final-state calculations with $\mathbf{g}_\parallel$-limited and $\mathbf{g}_\parallel$-unlimited conditions, respectively. (i), (j) Simulated spectra corresponding to (d) and (e) using the FP final states, respectively.

synchrotron ARPES measurements; the spectrum peaks for the s-polarization measurements appeared outside, while those for the p-polarization were inside [Figs. 3(d) and 3(e)]. Furthermore, we observed these peak positions oscillated continuously with the change in θ [Fig. S15(c) in SM [24]]. These behaviors were also well reproduced in simulations using the FP final states [Figs. 3(i), 3(j), and S16(a)–S16(c) in SM [24]]. In contrast, the PW final states exhibited worse agreement with the p-polarization spectra and the smoothness of the θ dependence curves [Figs. S16(d)–S16(f) in SM [24]]. To summarize, the FP final states agreed better with both synchrotron and low-energy laser ARPES results than the PW final states.

Finally, we analyze the FP wave functions to quantitatively show that they include various plane waves. For this analysis, we consider the case when the in-plane wavevector, the binding energy, and the excitation energy are (0.1, 0.0) (Å^{-1}), 0 eV (Fermi level), and 37 eV, respectively, corresponding to Fig. 3(g). From Eq. (2), the FP wave function includes waves with wavevector $\mathbf{k}_n + \mathbf{g} = (\mathbf{k}_\parallel + \mathbf{g}_\parallel) + (k_{nz} + g_z) - i\kappa_{nz}$ and amplitude $|p_n \psi_{n\mathbf{g}}|$. Figures 4(a) and 4(b) show the histogram of these amplitudes for $\mathbf{g}_\parallel = \bar{\Gamma}_0, \bar{\Gamma}_1$ [defined in Fig. 1(d)] and $\kappa_{nz} = 0$; $\kappa_{nz} \neq 0$ waves have only negligible amplitudes (Fig. S17 in SM [24]). While a prominent peak may be associated with the photoelectron wavevector of the three-step model, other components with different k_z values exist, each having amplitudes of at most 0.1. Furthermore, the wave function includes components with $k_z < 0$ (reflected waves) and $\mathbf{g}_\parallel = \bar{\Gamma}_1$ (different in-plane wavevector). While the former is explained using the stepped potential model, as we discuss in the Introduction, the latter is not and is due to the uneven crystal potential. The amplitude for larger $\mathbf{g}_\parallel$ is at most 0.01 (Fig. S18 in SM [24]), consistent with no large difference observed between the $\mathbf{g}_\parallel$-limited and $\mathbf{g}_\parallel$-unlimited calculations [Fig. 3(h)]. For further analysis, Fig. 4(c)

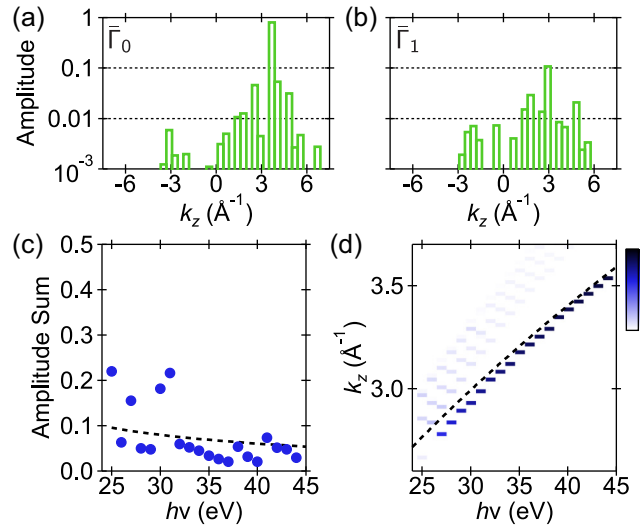

FIG. 4. Amplitude analysis of the FP wave function. (a), (b) Amplitude histogram for $\mathbf{g}_\parallel = \bar{\Gamma}_0, \bar{\Gamma}_1$. (c) Amplitude sum of the reflected ($k_z < 0$) waves in (a) and its photon energy dependence. The dashed curve represents the theoretical value of the stepped potential model. (d) Photon energy dependence of the amplitude histogram around the prominent peak. The dashed curve represents the k_z value of the three-step model.

compares the amplitude sum of the reflected waves and the theoretical value of the stepped potential model. Our simulation and the stepped potential model show similar degrees of amplitudes and decreasing behavior with respect to the photon energy. The prominent peak in the amplitude histogram can be compared with the k_z value of the three-step model [Fig. 4(d)]. A slight deviation is evident when the photon energy is around 30 eV, but it disappears around 40 eV. Such behavior is attributed to the higher photoelectron kinetic energy, that renders the potential unevenness more negligible. These results show that our FP wave functions share common characteristics with the stepped potential model and the three-step model, although they might seem too simple to reproduce the experimental ARPES spectra. We note that this analysis does not consider the decay function related to the ARPES surface sensitivity. While the disagreement between ARPES experiments and calculations has been reported [30,50], they will be mainly affected by the decay function, particularly its length scale.

In conclusion, we develop a numerical method to calculate the FP final states from the local Kohn-Sham potential. Leveraging the periodic property of the slab potential, we construct the wave function using the bulk eigenstates. We performed ARPES measurements on the transition metal dichalcogenide $1T$-TiS_2 and compared the photon-energy- and light-polarization-dependent results with simulations using our calculated FP final states and the PW final states. We revealed that the FP final states include various plane waves such as reflected ($k_z < 0$) waves and those with different in-plane wavevector ($\mathbf{g}_\parallel \neq 0$), and they contributed to a better coincidence between experiments and simulations. Our result can fill the gap between experiments and simplified simulations, which may connect the ARPES intensity distribution with the detail of the electronic structure, such as orbital components and the Berry phase. While we demonstrate that our method is better than the plane-wave approximation, we hope that further research compares the availability of various photoemission simulations beyond the plane-wave approximation in more detail, including ours and one using TR-LEED states with the imaginary optical potential correction [25–29] or plane waves modified by the scattering [17–19].

Acknowledgments. This work was supported by Grant-in-Aid for JSPS Fellows (Grant No. JP21J20657), Grant-in-Aid for Early-Career Scientists (Grant No. JP23K13041), Grant-in-Aid for Challenging Research (Pioneering) (Grants No. JP21K18181 and No. JP23K17351), Grant-in-Aid for Scientific Research (B) (Grant No. JP22H01943), Grant-in-Aid for Transformative Research Areas (A) (Grant No. JP21H05236), Grant-in-Aid for Scientific Research (A) (Grants No. JP19H00651, No. JP21H04439, and No. JP21H04652), the Asahi Glass Foundation, the Murata Science Foundation, and Collaborative Research Projects of Laboratory for Materials and Structures, Tokyo Institute of Technology. Laue back-reflection measurements were performed using the facilities of the Materials Design and Characterization Laboratory at the Institute for Solid State Physics, the University of Tokyo. The synchrotron radiation experiments were performed with the approval of Hiroshima Synchrotron Radiation Center (HiSOR) (Proposal No. 22BG046).

[1] J. A. Sobota, Y. He, and Z.-X. Shen, Rev. Mod. Phys. **93**, 025006 (2021).
[2] H. Hertz, Ann. Phys. **267**, 983 (1887).
[3] R. P. Day, B. Zwartsenberg, I. S. Elfimov, and A. Damascelli, npj Quantum Mater. **4**, 54 (2019).
[4] M. Yi, H. Pfau, Y. Zhang, Y. He, H. Wu, T. Chen, Z. R. Ye, M. Hashimoto, R. Yu, Q. Si, D.-H. Lee, P. Dai, Z.-X. Shen, D. H. Lu, and R. J. Birgeneau, Phys. Rev. X **9**, 041049 (2019).
[5] Y. H. Wang, D. Hsieh, D. Pilon, L. Fu, D. R. Gardner, Y. S. Lee, and N. Gedik, Phys. Rev. Lett. **107**, 207602 (2011).
[6] C. Hwang, C.-H. Park, D. A. Siegel, A. V. Fedorov, S. G. Louie, and A. Lanzara, Phys. Rev. B **84**, 125422 (2011).
[7] Y. Liu, G. Bian, T. Miller, and T.-C. Chiang, Phys. Rev. Lett. **107**, 166803 (2011).
[8] M. Schüler, U. D. Giovannini, H. Hübener, A. Rubio, M. A. Sentef, and P. Werner, Sci. Adv. **6**, eaay2730 (2020).
[9] E. L. Shirley, L. J. Terminello, A. Santoni, and F. J. Himpsel, Phys. Rev. B **51**, 13614 (1995).
[10] H. Daimon, S. Imada, H. Nishimoto, and S. Suga, J. Electron Spectrosc. Relat. Phenom. **76**, 487 (1995).
[11] H. Nishimoto, T. Nakatani, T. Matsushita, S. Imada, H. Daimon, and S. Suga, J. Phys.: Condens. Matter **8**, 2715 (1996).
[12] H. Nishimoto, T. Okuda, T. Nakatani, H. Daimon, T. Matsushita, S. Imada, S. Suga, H. Namba, T. Ohta, Y. Kagoshima, and T. Miyahara, Solid State Commun. **98**, 671 (1996).
[13] T. Matsushita, S. Imada, H. Daimon, T. Okuda, K. Yamaguchi, H. Miyagi, and S. Suga, Phys. Rev. B **56**, 7687 (1997).
[14] S. Moser, J. Electron Spectrosc. Relat. Phenom. **214**, 29 (2017).
[15] H. Tanaka, K. Kuroda, and T. Matsushita, J. Electron Spectrosc. Relat. Phenom. **264**, 147297 (2023).
[16] U. De Giovannini, H. Hübener, and A. Rubio, J. Chem. Theory Comput. **13**, 265 (2017).
[17] C. S. Kern, A. Haags, L. Egger, X. Yang, H. Kirschner, S. Wolff, T. Seyller, A. Gottwald, M. Richter, U. De Giovannini, A. Rubio, M. G. Ramsey, F. C. Bocquet, S. Soubatch, F. S. Tautz, P. Puschnig, and S. Moser, Phys. Rev. Res. **5**, 033075 (2023).
[18] P. Krüger, F. Da Pieve, and J. Osterwalder, Phys. Rev. B **83**, 115437 (2011).
[19] P. Krüger and F. Matsui, J. Electron Spectrosc. Relat. Phenom. **258**, 147219 (2022).
[20] S. Hüfner, *Photoelectron Spectroscopy* (Springer, Berlin, 2003).
[21] H. Tanaka, e-J. Surf. Sci. Nanotechnol. **21**, 139 (2022).
[22] I. Adawi, Phys. Rev. **134**, A788 (1964).
[23] G. D. Mahan, Phys. Rev. B **2**, 4334 (1970).
[24] See Supplemental Material at http://link.aps.org/supplemental/10.1103/PhysRevB.109.L241114 for experimental and calculation conditions and additional data supporting our arguments, which includes Refs. [31–44].
[25] E. E. Krasovskii and W. Schattke, Phys. Rev. Lett. **93**, 027601 (2004).

[26] V. N. Strocov, E. E. Krasovskii, W. Schattke, N. Barrett, H. Berger, D. Schrupp, and R. Claessen, Phys. Rev. B **74**, 195125 (2006).
[27] E. E. Krasovskii, V. N. Strocov, N. Barrett, H. Berger, W. Schattke, and R. Claessen, Phys. Rev. B **75**, 045432 (2007).
[28] J. Schusser, H. Bentmann, M. Ünzelmann, T. Figgemeier, C.-H. Min, S. Moser, J. N. Neu, T. Siegrist, and F. Reinert, Phys. Rev. Lett. **129**, 246404 (2022).
[29] V. N. Strocov, L. L. Lev, F. Alarab, P. Constantinou, X. Wang, T. Schmitt, T. J. Z. Stock, L. Nicolaï, J. Očenášek, and J. Minár, Nat. Commun. **14**, 4827 (2023).
[30] H. Tanaka, S. Okazaki, M. Kobayashi, Y. Fukushima, Y. Arai, T. Iimori, M. Lippmaa, K. Yamagami, Y. Kotani, F. Komori, K. Kuroda, T. Sasagawa, and T. Kondo, Phys. Rev. Lett. **132**, 136402 (2024).
[31] D. A. Shirley, Phys. Rev. B **5**, 4709 (1972).
[32] X. Chen, M. Song, L. Zhang, R. Zhang, L. Zhang, W. Tong, Y. Han, X. Gao, Y. Xiong, H. Xu, and L. Cao, J. Phys. Chem. C **127**, 3462 (2023).
[33] E. N. Maslen, A. G. Fox, and M. A. O'Keefe, in *International Tables for Crystallography*, edited by E. Prince (Wiley, Hoboken, NJ, 2006), Vol. C, Chap. 6.1.1, pp. 554–590.
[34] T. Ozaki, Phys. Rev. B **67**, 155108 (2003).
[35] P. Giannozzi, S. Baroni, N. Bonini, M. Calandra, R. Car, C. Cavazzoni, D. Ceresoli, G. L. Chiarotti, M. Cococcioni, I. Dabo, A. D. Corso, S. de Gironcoli, S. Fabris, G. Fratesi, R. Gebauer, U. Gerstmann, C. Gougoussis, A. Kokalj, M. Lazzeri, L. Martin-Samos *et al.*, J. Phys.: Condens. Matter **21**, 395502 (2009).
[36] P. Giannozzi, O. Andreussi, T. Brumme, O. Bunau, M. B. Nardelli, M. Calandra, R. Car, C. Cavazzoni, D. Ceresoli, M. Cococcioni, N. Colonna, I. Carnimeo, A. D. Corso, S. de Gironcoli, P. Delugas, R. A. DiStasio, A. Ferretti, A. Floris, G. Fratesi, G. Fugallo *et al.*, J. Phys.: Condens. Matter **29**, 465901 (2017).
[37] We used the pseudopotentials Ti.pbe-spn-rrkjus_psl.1.0.0.UPF and S.pbe-n-rrkjus_psl.1.0.0.UPF from PSlibrary: https://dalcorso.github.io/pslibrary/.
[38] J. P. Perdew, K. Burke, and M. Ernzerhof, Phys. Rev. Lett. **77**, 3865 (1996).
[39] J. P. Perdew, K. Burke, and M. Ernzerhof, Phys. Rev. Lett. **78**, 1396(E) (1997).
[40] J. Heyd, G. E. Scuseria, and M. Ernzerhof, J. Chem. Phys. **118**, 8207 (2003).
[41] J. Heyd, G. E. Scuseria, and M. Ernzerhof, J. Chem. Phys. **124**, 219906 (2006).
[42] G. Pizzi, V. Vitale, R. Arita, S. Blügel, F. Freimuth, G. Géranton, M. Gibertini, D. Gresch, C. Johnson, T. Koretsune, J. Ibañez-Azpiroz, H. Lee, J.-M. Lihm, D. Marchand, A. Marrazzo, Y. Mokrousov, J. I. Mustafa, Y. Nohara, Y. Nomura, L. Paulatto *et al.*, J. Phys.: Condens. Matter **32**, 165902 (2020).
[43] A. Stoliaroff, S. Jobic, and C. Latouche, Inorg. Chem. **58**, 1949 (2019).
[44] M. Marsman, J. Paier, A. Stroppa, and G. Kresse, J. Phys.: Condens. Matter **20**, 064201 (2008).
[45] P. Hohenberg and W. Kohn, Phys. Rev. **136**, B864 (1964).
[46] W. Kohn and L. J. Sham, Phys. Rev. **140**, A1133 (1965).
[47] W. Jin, P.-C. Yeh, N. Zaki, D. Zhang, J. T. Sadowski, A. Al-Mahboob, A. M. van der Zande, D. A. Chenet, J. I. Dadap, I. P. Herman, P. Sutter, J. Hone, and R. M. Osgood, Phys. Rev. Lett. **111**, 106801 (2013).
[48] P. Chen, Y.-H. Chan, X.-Y. Fang, Y. Zhang, M. Y. Chou, S.-K. Mo, Z. Hussain, A.-V. Fedorov, and T.-C. Chiang, Nat. Commun. **6**, 8943 (2015).
[49] H. Tanaka, S. Okazaki, K. Kuroda, R. Noguchi, Y. Arai, S. Minami, S. Ideta, K. Tanaka, D. Lu, M. Hashimoto, V. Kandyba, M. Cattelan, A. Barinov, T. Muro, T. Sasagawa, and T. Kondo, Phys. Rev. B **105**, L121102 (2022).
[50] D. Huang, H. Nakamura, K. Küster, U. Wedig, N. B. M. Schröter, V. N. Strocov, U. Starke, and H. Takagi, Phys. Rev. B **105**, 245145 (2022).
[51] F. Matsui and S. Suga, Phys. Rev. B **105**, 235126 (2022).
[52] J. A. Wilson, F. J. Di Salvo, and S. Mahajan, Phys. Rev. Lett. **32**, 882 (1974).
[53] K. Yaji, A. Harasawa, K. Kuroda, S. Toyohisa, M. Nakayama, Y. Ishida, A. Fukushima, S. Watanabe, C. Chen, F. Komori, and S. Shin, Rev. Sci. Instrum. **87**, 053111 (2016).
[54] K. Kawaguchi, K. Kuroda, Z. Zhao, S. Tani, A. Harasawa, Y. Fukushima, H. Tanaka, R. Noguchi, T. Iimori, K. Yaji, M. Fujisawa, S. Shin, F. Komori, Y. Kobayashi, and T. Kondo, Rev. Sci. Instrum. **94**, 083902 (2023).
[55] M. P. Seah and W. A. Dench, Surf. Interface Anal. **1**, 2 (1979).
[56] I. Morrison, D. M. Bylander, and L. Kleinman, Phys. Rev. B **47**, 6728 (1993).